*J. Fluid Mech.* (2019), *vol.* 875, *pp.* 842–853.  
doi:10.1017/jfm.2019.503

# Kinematics of vortex ring generated by a drop upon impacting a liquid pool

**Abhishek Saha[1,2,†], Yanju Wei[1,3], Xiaoyu Tang[1] and Chung K. Law[1]**

[1]Department of Mechanical and Aerospace Engineering, Princeton University, Princeton, NJ 08544, USA

[2]Department of Mechanical and Aerospace Engineering, University of California San Diego, La Jolla, CA 92093, USA

[3]School of Energy and Power Engineering, Xi'an Jiaotong University, Xi'an 710049, China

(Received 15 January 2019; revised 12 June 2019; accepted 17 June 2019; first published online 25 July 2019)

We herein report an experimental study on the morphological evolution of a vortex ring formed inside a liquid pool after it is impacted and penetrated by a coalescing drop of the same liquid. The dynamics of the penetrating vortex ring along with the deformation of the pool surface has been captured using simultaneous high-speed laser induced fluorescence and shadowgraph techniques. It is identified that the motion of such a vortex ring can be divided into three stages, during which inertial, capillary and viscous effects alternatingly play dominant roles to modulate the penetration process, resulting in linear, non-monotonic and decelerating motion in these three stages respectively. Furthermore, we also evaluate the relevant time and length scales of these three stages and subsequently propose a unified description of the downward motion of the penetrating vortex ring. Finally, we use the experimental data for a range of drop diameters and impact speeds to validate the proposed scaling.

**Key words:** drops, breakup/coalescence, vortex dynamics

## 1. Introduction

Drop impact on a liquid film of various depths and the subsequent penetration and mixing is critical in many natural and industrial processes, including, for example, rainfall on the ocean surface (Prosperetti, Crum & Pumphrey 1989), inkjet printing (van der Bos *et al.* 2014), fuel spray in internal combustion engines (Moreira, Moita & Panao 2010) and spray for cooling, coating and agriculture (Aziz & Chandra 2000; Gart *et al.* 2015; Gilet & Bourouiba 2015). Consequently, drop impact on liquid surfaces has been a major topic in fluid dynamics research, with recent reviews by Rein (1993), Josserand & Thoroddsen (2016) and Yarin (2006). Much of these previous studies have focused on events at the air–liquid interface, such as the transition between bouncing–merging (Rein 1993; Tang *et al.* 2016, 2018; Weheliye, Dong & Angeli 2017); formation of central jetting (Rein 1993, 1996; Zhao, Brunsvold & Munkejord 2011; Castillo-Orozco *et al.* 2015; Michon, Josserand & Séon 2017); onset and dynamics of splashing and crown formation

† Email address for correspondence: asaha@eng.ucsd.edu

(Rein 1993; Weiss & Yarin 1999; Thoroddsen 2002; Yarin 2006; Deegan, Brunet & Eggers 2007); dynamics of crater formation (Rein 1993; Yarin 2006; Michon *et al.* 2017); evolution of interfacial gas layer dynamics and bubble entrapment (Thoroddsen, Etoh & Takehara 2003; Bird *et al.* 2010; Thoraval *et al.* 2013; Beilharz *et al.* 2015; Murphy *et al.* 2015; Michon *et al.* 2017; Tang *et al.* 2019).

However, the long-term developments occurring under the air–liquid interface, involving the penetration and mixing of the drop in the impacted pool, are relatively less explored. Several studies (Chapman & Critchlow 1967; Peck & Sigurdson 1994; Dooley *et al.* 1997) have looked into the evolution of the vortex ring created by the merging of the drop and the impacted liquid pool. For a narrow range of impact conditions, Peck & Sigurdson (1994) proposed a theoretical model to construct the topology of the vortex ring. Furthermore, Chapman & Critchlow (1967) and Peck & Sigurdson (1994) investigated the role of sphericity of the drop on the characteristics of the vortex ring, and found that spherical droplets, oscillating from oblate to prolate shape, generate the maximum penetration. Rodriguez & Mesler (1988), however, reported that the largest penetration of the vortex ring occurred for prolate droplets, and *vice versa*. Working with vanishing velocity impacts, Shankar & Kumar (1995) and Dooley *et al.* (1997) showed that the penetration process is solely controlled by the capillarity or surface energy of the droplet, which may not hold for finite impact velocities. In light of the valuable qualitative and phenomenological understanding gained on the overall dynamics of the motion of the submerged drop from the above studies, quantitative evaluation and physical reasoning of its kinematics is nevertheless not well understood. In response to such a need we report herein an experimental study to characterize the kinematics of the vortex ring generated by the submerged drop impacting on a liquid pool, and to identify the various competing factors that control its motion at different stages of the penetration. By using high-speed laser induced fluorescence, we have captured the spatial and temporal evolution of the motion and the overall morphology, and subsequently identified the similarity between the penetration processes for drops of different sizes and impact velocities. We shall now present the experimental set-up, followed by an analysis of the data to show that inertia, capillarity and viscous drag control the drop motion at various stages. Finally, we shall derive a unified expression to describe the penetration process.

## 2. Experimental set-up

The drop in our experiment was generated by slowly pushing the liquid through a vertically suspended needle using a syringe pump, as shown in figure 1(*a*). When the drop becomes larger than a critical size, it detaches from the needle tip and subsequently falls downwards to land on the liquid film hosted in a 50 mm $\times$ 50 mm $\times$ 30 mm rectangular glass chamber. The drop size and impact speed were modulated by changing the needle diameter and the distance between the film surface and the needle, respectively. To observe the post-impact motion of the drop inside the liquid pool, high-speed laser induced fluorescence (LIF) was performed by doping the drop liquid with a trace amount ($<$0.01 % mass fraction) of Rhodamine-6G dye, while leaving the liquid pool un-dyed. A Nd-YLF high-speed (527 nm) laser along with the required optics was used to create a 500 $\mu$m thick laser sheet which passes through the centre of the liquid reservoir. Using a three-dimensional traverse system, the needle was precisely positioned such that the drop lands on the liquid pool where the laser sheet centrally intersects. A synchronized high-speed camera with a bandpass filter recorded the fluorescence images from the drop. A 550 nm

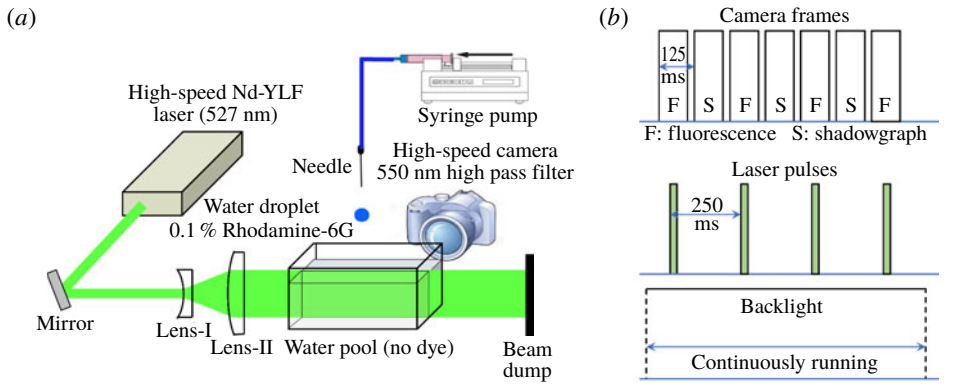


FIGURE 1. (Colour online) (*a*) Experimental set-up. (*b*) Timing diagram demonstrating how LIF was captured in every alternate image.

high pass filter was used to capture the fluorescence signal while removing the laser line (527 nm) and the stray lights from these images. A separate backlight was used to capture the structure of the dynamics of the pool surface through shadowgraphy. An external timing unit was used to synchronize the high-speed camera, recording at 8 kHz framing rate with the laser pulsing at 4 kHz, such that fluorescence was synchronized with alternate recorded images, while the other half of the images captured the shadowgraph. Thus, as shown through the timing sequence in figure 1(*b*), the effective recording speed for both the LIF images and shadowgraph was 4 kHz.

De-ionized (DI) water (density, $\rho = 998$ kg m$^{-3}$, surface tension, $\sigma = 70$ mN m$^{-1}$ and dynamic viscosity, $\mu = 1$ mPa s) was used as liquid for the drop and the pool, since Rhodamine6G is easily soluble. The amount of dye dissolved in water used in the experiments is sufficiently small ($<0.01\,\%$ mass fraction) that no discernible change was observed in the liquid properties. A large film/pool thickness, $H$, which was ten times the drop radius, was used to alleviate effects of the bottom substrate on the penetration and vortex dynamics. Three different drop diameters ($D \approx 2$, 3, 3.5 mm) and a large range of Weber numbers ($We$), from 5 to 40, were used to cover a wide range of capillary time ($\tau_c \in [7.7\text{–}19.7$ ms]) and inertial time ($\tau_i \in [2.4\text{–}8.2$ ms]) scales. Here, the Weber number is defined as $We = \rho U^2 D/\sigma$, where $U$ and $D$ are the impact velocity and diameter of the drop, which are calculated from shadowgraph images before the impact. In the following analyses, two fundamental time scales, namely the inertial time scale of the drop ($\tau_i = D/U$) and the capillary time scale of the pool ($\tau_c = 2\pi/\omega_c$) will be used. Here, $\omega_c$ is the capillary frequency, which for the deep pool ($H \gg D$) can be expressed as $\omega_c = \sqrt{(64\sigma)/(\rho D^3)}$ (Pan & Law 2007; Kundu & Cohen 2008).

It is noted that for impact velocities smaller than a critical value, the impacting drop can bounce from the liquid surface due to the resistance from the trapped interfacial gas layer between the drop and film surface (Tang *et al.* 2016, 2019), while splashing can occur for a sufficiently large impact velocity (Hsiao, Lichter & Quintero 1988; Leng 2001). Since we are interested in the motion of vortex ring generated by the merged drop, unaffected by splashing, our experiments were conducted with impact velocities that are sufficiently large to induce gas film rupture and the subsequent merging, but not too large to induce splashing.

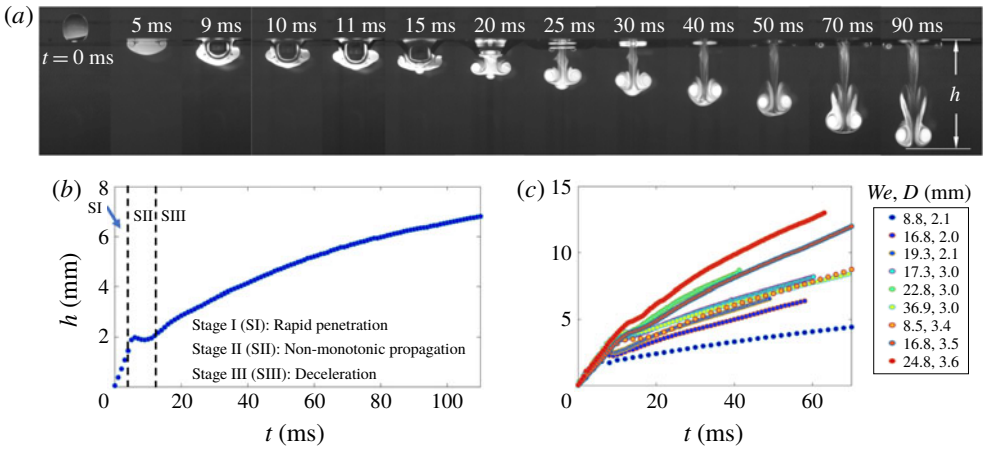


FIGURE 2. (Colour online) (*a*) Sequence of high-speed LIF images depicting the penetration process. (*b*) Penetration history of one experiment ($We = 10.2$, $D = 1.9$ mm). (*c*) Penetration history for a series of experiments, $D \in [2, 3, 3.5 \text{ mm}]$, $We \in [8 : 37]$.

## 3. Results

### 3.1. *General dynamics*

The motion of a merged drop during a typical impact process is illustrated through a series of fluorescence images, shown in figure 2(*a*), which demonstrate several notable characteristics. Specifically, at the very early stage of the impact, when the drop starts penetrating into the stagnant liquid pool, a vortex ring is generated around the outer periphery of the drop due to the large shear rate (figure 2*a*, $t = 5$ ms), and becomes larger as the drop penetrates into the pool. As the rear end of the drop falls below the liquid surface, a crater is developed on the surface of the pool, which pushes the drop downwards until the crater on the liquid surface reaches a maximum depth and subsequently starts relaxing (figure 2*a*, $t = 20$ ms) to regain its original unperturbed state. The spread of the vortex ring then becomes smaller as the vortices approach each other and continue the penetration.

Among the various dynamic and characteristic analyses that can be performed on this process, here we are mostly interested in the overall downward motion and penetration of the vortex ring. Specifically, the primary quantity of interest is the penetration depth, $h$, which is the distance between the bottom-most point of the vortex ring, marked by the dye, and the unperturbed liquid surface, as defined in figure 2(*a*). The temporal evolution of $h$ is plotted for a typical experiment in figure 2(*b*), from which we can clearly identify three distinct stages of the penetration process. Here, $t = 0$ is the instant when the drop touches the unperturbed liquid pool. At the early stage immediately after the impact, a steady increase of $h(t)$ with almost a constant slope is observed. The motion in this stage I, termed 'Rapid penetration', is primarily controlled by the impact inertia and as such the slope is almost constant. On the other hand, far from impact in stage III of 'Deceleration', we observe a monotonic penetration process with steady deceleration, marked by a continuous decay in the slope, caused by the viscous effect. Interestingly, at the intermediate or transitional period between stages I and III, the drop motion shows a non-monotonic penetration process, in that $h(t)$ first increases and then slightly decreases with time, exhibiting an oscillatory motion. Such a behaviour in this stage II, termed as

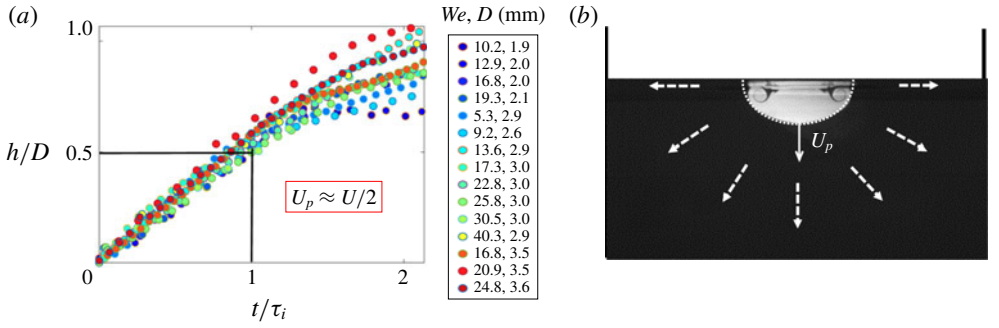


FIGURE 3. (Colour online) (*a*) Inertial stage: normalized penetration history at early stage of penetration. (*b*) Schematic of the radial flow in liquid pool induced by the penetrating drop.

'Non-monotonic propagation', is caused by the crater on the pool surface created by the impact. Evolution of the penetration depth is compared for various $D$ and $We$ in figure 2(*c*), which does not show any similarity between different stages in different experiments, suggesting that the three stages are characterized by different length and time scales. We now explore the varying extent of influence of these three major effects, i.e. impact inertia, viscous drag and capillarity, in the drop motion in these stages and show how their influence can be scaled.

### 3.2. *Inertial effect*

Immediately after impact, penetration is dominated by the impact inertia of the drop. At this stage the drop kinetic energy is dominant, and the flow induced in the pool is mostly radial in nature with minimal dissipation. Recognizing that the Reynolds number of the drop is high and that the capillary disturbance of the pool surface is minimal, we expect viscous and capillary effects to be weak during this stage. Also, the Froude number $(U/\sqrt{gD/2})$ for our experiments is greater than unity, showing a negligible effect of gravity. Thus, the penetration at this stage is controlled by the impact inertia. This is also evident from the linear nature of the penetration history in stage I, shown in a non-dimensional plot (figure 3*a*), where $t$ is normalized by the inertial time scale, $\tau_i$, and $h(t)$ is normalized by the drop diameter, $D$. In figure 3(*a*), we notice that for a wide range of $D$ and $We$, the normalized penetration histories collapse to a linear fit until $t/\tau_i \approx 1$, beyond which they diverge, confirming the dominant role of impact inertia in stage I. Moreover, the slope of the normalized data is close to 1/2, which suggests that the penetration velocity, $U_p(=\mathrm{d}h/\mathrm{d}t)$, defined as the velocity at which the coalesced drop front is moving inside the pool, is half of the impact velocity, $U_p \approx U/2$. This loss in kinetic energy can be attributed to the motion induced in the pool, due to the drop impact. Using energy budget analyses for the unmerged drop, Tran *et al.* (2013) and Tang *et al.* (2016) showed that the kinetic energy of the induced flow $(E_{k,l})$ in the pool is approximately 3/4 of the initial drop kinetic energy, $E_{k,0} = (1/12)\pi\rho D^3 U^2 \sim U^2$. Considering the drop kinetic energy after the impact is $E_{k,p} \sim U_p^2$, the energy balance before and after the impact, i.e. $E_{k,0} = E_{k,p} + E_{k,l}$, results in $E_{k,p} \approx (1/4)E_{k,0}$ or $U_p \approx (1/2)U$. Note that this result can alternatively be obtained by following Wagner's theory in the context of a drop impacting a shallow pool, as shown in Purvis & Smith (2005). Finally, from our

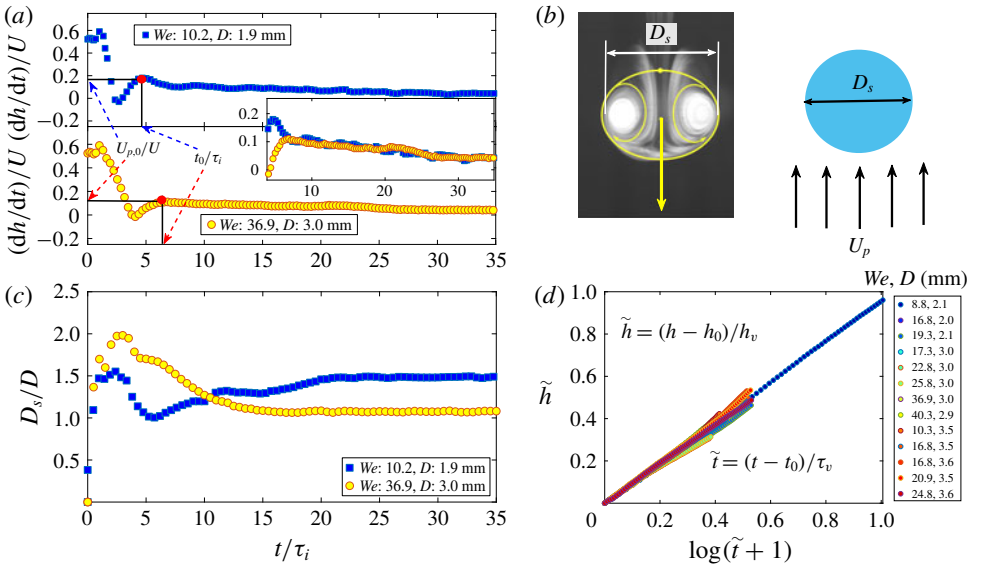


FIGURE 4. (Colour online) (*a*) Normalized penetration velocity $\mathrm{d}h_p/\mathrm{d}t$ as a function of normalized time, $t/\tau_i$. Inset: zoomed view of stage III showing the deceleration. (*b*) Drop far from the pool surface: assuming spherical geometry and defined diameter ($D_s$). (*c*) Normalized $D_s$ of the penetrating drop as a function of normalized time. $D_s$ becomes constant at the late stage of penetration. (*d*) $(h-h_0)/h_v$ as a function of $\ln[(t-t_0)/\tau_v + 1]$ for a wide range of *We* and *D*.

knowledge of the penetration speed for the inertial controlled stage I, the equation of motion in non-dimensional form can be expressed as

$$\frac{h(t)}{D} = \frac{1}{2}\frac{t}{\tau_i}, \quad \text{for } 0 \leqslant \frac{t}{\tau_i} \leqslant 1. \tag{3.1}$$

### 3.3. *Viscous drag*

During the late stage of the penetration, when the vortex ring is sufficiently far away from the liquid surface, it continues to move down with a steady deceleration, as seen in stage-III of figure 2(*b*). This deceleration in the late stage is also clearly visible if we plot the instantaneous normalized penetration velocity for two typical experiments (figure 4*a*). The penetration process in this stage almost resembles the motion of a sphere in a stagnant liquid, with the notable exception of the presence of a toroidal vortex ring (figure 4*b*). However, it is interesting to note that $D_s$, the virtual diameter of the sphere encompassing the vortex ring, remains almost constant at this stage, as shown for two different experiments in figure 4(*c*). Moreover, mixing of the dye with the surrounding liquid via the vortex is still not significant, and thus entrainment of the dye-free water from the pool is neglected here. The motion of the vortex ring, then, is modelled as a spherical mass moving through a stagnant liquid (figure 4*b*), and we can write $m(\mathrm{d}U_p/\mathrm{d}t) = -F_D = -C_D A_{cs}(\rho U_p^2/2)$, where $m = (\pi\rho D_s^3/6)$ is the mass of the fictitious sphere encompassing the vortex ring, $U_p = \mathrm{d}h/\mathrm{d}t$ the penetration velocity, $F_D$ the drag force, $C_D$ the drag coefficient and $A_{cs} = \pi D_s^2/4$ the cross-sectional area. By integrating the expression twice with the boundary conditions, $h(t = t_0) = h_0$ and

$U_p(t = t_0) = U_{p,0}$, we find

$$\frac{h(t) - h_0}{h_v} = \ln\left[\frac{t - t_0}{\tau_v} + 1\right], \tag{3.2}$$

where, $h_v = (4D_s)/(3C_D)$ and $\tau_v = (4D_s)/(3C_D U_{p,0})$. It can be seen that $h_v (\sim D_s)$ and $\tau_v (\sim D_s/U_{p,0})$ are the effective length and time scales for this stage. In the current experiments, $\tau_v$ ranges from 46.1 to 120.5 ms. We identify $t_0$ as the time when the penetration velocity $\mathrm{d}h/\mathrm{d}t$ attains a local maximum and the subsequent penetration process displays a monotonic decrease in $\mathrm{d}h/\mathrm{d}t$, as shown in figure 4(*a*). Subsequently, the $t_0$, $h_0$ and $U_{p,0}$ values are extracted from individual experiments. The effective Reynolds number ($Re = \rho U_p D_s/\mu$) at this stage is approximately $10^3$–$10^4$, and for which the drag coefficient $C_D$, for flow over a smooth sphere, has a value close to 0.5 (NASA 1999; Kundu & Cohen 2008). Alternatively, a 'best-fit' value of $C_D$ for each condition can also be obtained by comparing the experimental data with the theoretical prediction in (3.2). These individual 'best-fit' $C_D$ values are also found to have values close to 0.5 (details in supplementary material available online at https://doi.org/10.1017/jfm.2019.503). Consequently, we use $C_D = 0.5$ for all the experimental conditions and plot $(h - h_0)/h_v$ as a function of $\ln[(t - t_0)/\tau_v + 1]$ in figure 4(*d*), which shows very close resemblance with the scaling. It is noted that (3.2) represents an exact solution, which does not require any proportionality constant, as supported by the near-unity slope in figure 4(*d*). In passing, we further note that for the current experiments $(D_s g)/(2C_D U_p^2)$ is less than unity, suggesting that the gravity effect is negligible compared to that of viscous drag.

### 3.4. *Capillary effect*

Capillary effect of the pool surface plays a critical role in the intermediate stage, which is marked by the non-monotonic changes in $h$ versus $t$ (figure 2*b*). This oscillation is caused by the formation (and relaxation) of the crater on the pool surface (figure 2*a*, $t > 5$ ms) due to the impact. The crater eventually reaches a maximum depth due to the capillary effect, and then the highly distorted pool surface retracts to attain its original shape (figure 5*a*). The formation and retraction of the crater induce an additional downward and upward motion respectively, in the pool, which periodically accelerates and decelerates the penetration of the vortex ring visible through oscillations in stage II, as seen in figure 2(*b*). The primary two parameters, which characterize the formation and relaxation of the pool surface, are the maximum crater depth $H_{md}$ and the time $t_{md}$ taken (after the initial contact between the drop and the pool surface) to create this maximum crater depth. In figure 5(*b*), we plot $t_{md}$ normalized by the capillary time scale of the pool surface, $\tau_c$, and it is found to be almost constant (figure 5*b*) for all the experiments across different drop sizes and impact velocities. This confirms that the process is controlled by capillarity and the effects of inertia are minimal. On the other hand, if plotted with $We$ in figure 5(*c*), the non-dimensional $H_{md}$, normalized by $D$, displays a power law dependence with an exponent close to 0.5, i.e. $H_{md}/D \sim We^{1/2}$ (figure 5*c*). Such a power law dependence can be explained by an energy balance assuming that the kinetic energy of the penetrating drop, $E_{k,p} = \pi\rho D^3 U_p^2/12$, has been converted to the surface energy of the crater, $E_{s,H}$, and we have already shown that $U_p = 1/2U$. Furthermore, we assume that the crater has a hemispherical shape, shown in figure 5(*d*), whose surface area is $A_{Hd} \approx 2\pi H_{md}^2$. This leads to $E_{s,H} = \sigma A_{Hd} \approx 2\sigma\pi H_{md}^2$, or $H_{md}/D \sim We^{1/2}$, which is

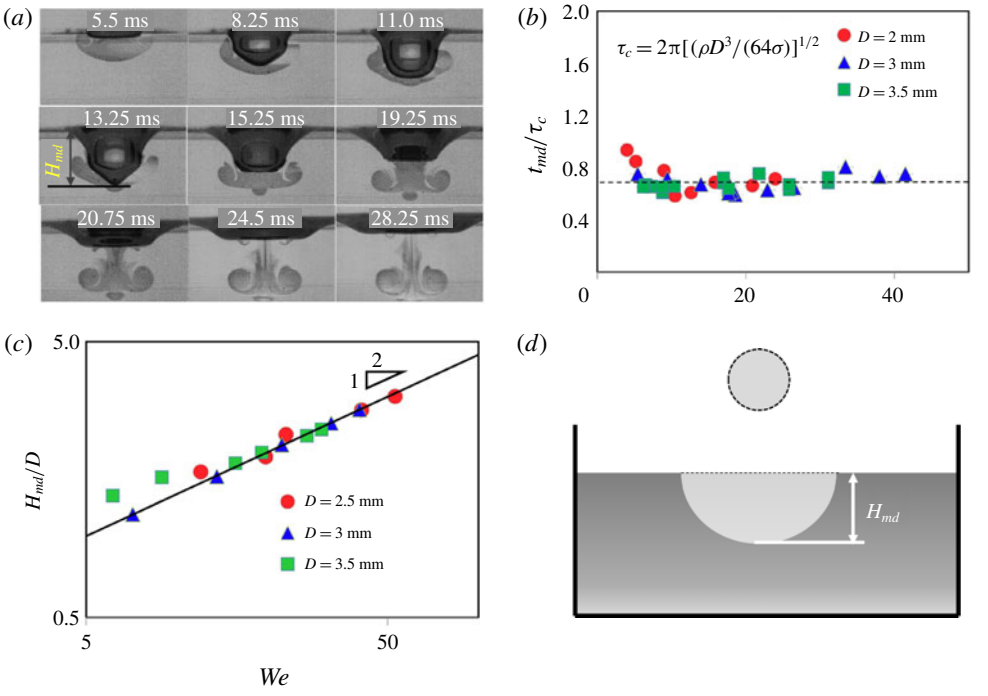


FIGURE 5. (Colour online) (*a*) Shadowgraph image: formation and relaxation of the crater. The dark region is the crater. The maximum crater depth, $H_{md}$ is also identified. (*b*) Non-dimensional crater formation time as a function of *We* for three different drop diameters. (*c*) Non-dimensional maximum crater depth as a function of *We* in log–log scale. (*d*) Schematic of the crater formation.

closely supported by the experimental data shown in figure 5(*c*). The scalings of $H_{md}$ and $t_{md}$ confirm that the crater formation process is capillarity driven. It is also noted that for the present experiments, the Bond number, $Bo = [(\rho g)/(\sigma k^2)]$ is less than unity, suggesting that the capillary wave is stronger than the gravity wave and as such the latter has been neglected.

To evaluate the effect of crater formation on the penetration of the vortex ring, we first formulate the crater formation process, which can be expressed as a capillary wave moving through the surface of the pool. The beginning of crater formation is marked by the instant when the rear end of the drop (outside the pool), moving with velocity $U$, reaches the unperturbed liquid surface, i.e. at $t = \tau_i$, which also represents the end of stage I. Since the crater formation is a capillary driven process, its effect on the penetration velocity of the drop can be expressed as $U_c = U_p \cos[\omega_c(t - \tau_i)]$ and its effect on the penetration depth as $h_{p,c} = (U_p/\omega_c) \sin[\omega_c(t - \tau_i)]$. The influence of the capillary wave, as manifested by the formation and relaxation of the crater, will be felt by the vortex ring, as long as it is in close vicinity to the pool surface. Although one can expect that the transition to the next stage will occur between 1/4 of the capillary period when the capillary deformation is maximum, and 1/2 of the capillary period when the pool surface reaches its initial state during the retraction process, the exact duration of the capillary effect on penetration, i.e. duration of stage II, is difficult to ascertain simply from scaling. However, as shown in figure 4(*c*), from experiments we can identify $t = t_0$, beyond which the penetration velocity monotonically decreases due

to a pure viscous effect without any effect of capillary oscillation in the pool surface. Thus, we use $t = t_0$ as the end of stage II, where the capillary effect on penetration is important. Although capillarity has a strong effect on the drop motion in stage II, the viscous effect is equally important, as evident from the increasing mean position of the drop during this stage (figure 2*b*). It is noted that the relative contributions from the viscous and capillary effects to propagation during this stage are comparable (shown in supplementary materials), and hence the viscous term cannot be neglected. Recognizing that stage II includes both viscous and capillary effects, the equation of motion for this stage can be expressed as

$$\frac{h(t)}{D} = \frac{1}{2} + \frac{\tau_c}{\tau_i}\frac{1}{4\pi}\sin\left[2\pi\frac{t-\tau_i}{\tau_c}\right] + \frac{h_v}{D}\ln\left[\frac{t-\tau_i}{\tau_v}+1\right]. \tag{3.3}$$

## 4. Summary

In the present study we have explored the motion of a coalesced drop, after it impacts a liquid pool, to understand the controlling mechanisms that guide its motion inside the pool. Analysing the kinematics of the vortex ring through the high-speed laser induced fluorescence images, we identified three distinct stages of penetration, namely, rapid penetration, non-monotonic propagation and deceleration. Detailed analysis of each of these stages showed various extents of influence of the inertial, capillary and viscous effects. Specifically, at the very early stage of motion following the impact, penetration is dominated by the impact inertia and as such the vortex ring moves at a near-constant velocity. At the late stage of the penetration, the motion is controlled by viscous drag, which continuously decelerates the vortex ring. In the intermediate stage, characterized by non-monotonic motion, both capillary and viscous effects are important. The capillarity causes perturbation in the pool surface through crater formation, which drives a wave-like motion in the pool liquid affecting the penetration. Each of these effects at the individual stages are subsequently characterized and scaled with relevant quantities, which are supported by the experimental results. Since a kinematic equation of motion has been derived for each of these effects, we can now combine them to derive a piecewise kinematic equation for the entire penetration process. Recognizing that in stages I and III, inertia and viscous drag are respectively the sole dominant processes, in stage II both capillary and viscous effects are important and that the end of stages I and II are marked by $t = \tau_i$ and $t = t_0$, we can write

$$\frac{h(t)}{D} = \begin{cases} \dfrac{1}{2}\dfrac{t}{\tau_i} & : 0 \leqslant t \leqslant \tau_i \\ \dfrac{1}{2} + \dfrac{\tau_c}{\tau_i}\dfrac{1}{4\pi}\sin\left[2\pi\dfrac{t-\tau_i}{\tau_c}\right] + \dfrac{h_v}{D}\ln\left[\dfrac{t-\tau_i}{\tau_v}+1\right] & : \tau_i < t \leqslant t_0 \\ \dfrac{h_0}{D} + \dfrac{h_v}{D}\ln\left[\dfrac{t-t_0}{\tau_v}+1\right] & : t > t_0, \end{cases} \tag{4.1}$$

which describes the kinematics of the entire penetration process. It is noted that $\tau_i$ and $\tau_v$ are the characteristic time scales for stages I and III, respectively, while in stage II $\tau_i$, $\tau_c$ and $\tau_v$ are all important. Similarly, three different length scales, $D$, $h_0$ and $h_v$ are relevant at different stages. Owing to the presence of multiple length and time scales at different stages of this multiscale process, defining a single length or time scale is not appropriate.

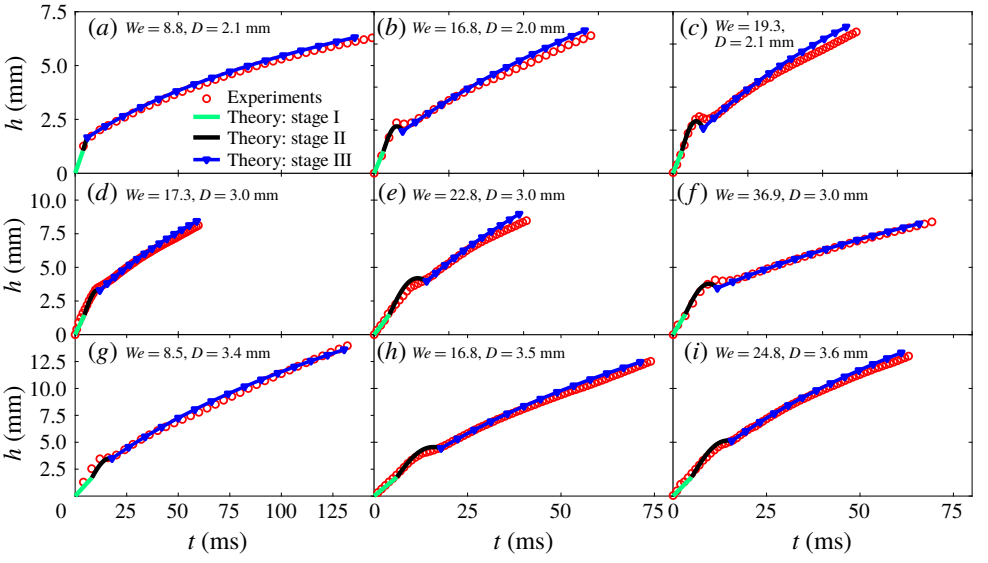


FIGURE 6. (Colour online) Comparison of experiments and scaling: penetration depth as function of time for a wide range of conditions.

We next compare the experimental data with the theoretical expression (4.1) in figure 6, where $h$ is plotted versus $t$ in dimensional space for three different $D$ and different $We$. It is seen that by changing the drop diameter, $D$, we are modulating both $\tau_i$ and $\tau_c$, while by changing the Weber number, $We$, we are modulating the ratio between them. Thus, the nine sets of experimental data presented in figure 6, represent nine different combinations of inertial ($\tau_i$) and capillary ($\tau_c$) conditions. The comparison shows a remarkable agreement between the experimental results and theoretical predictions, hence suggesting that the simple theory captures the physics controlling the penetration process. We recognize that while in experiments the transition from one stage to another occurs gradually over a finite time, the kinematic equations developed for the three stages are piecewise in nature, with a sharp instant transition. This introduces discrepancies between the model and the experiments near the transitions. Furthermore, for completeness we have also evaluated $\mathrm{d}h/\mathrm{d}t$ for these nine conditions, which also show three stages of propagation (see supplementary material). The values of $t_0$ and $h_0$ for these nine conditions are also reported in the supplementary material.

We conclude the present study by stating that, although the results are highly repeatable, we have considered only impacts for which the drop aspect ratio is relatively close to unity and the impact speed does not cause splashing. It is anticipated that non-sphericity in shape and splashing will significantly affect the initial vortex formation and the subsequent penetration, which require further studies.

**Acknowledgements**

The work at Princeton University was supported by the Army Research Office (grant no. W911NF1610449). Y.W. acknowledges the financial support from the China Scholarship Council (CSC no. 201606285074) for his sabbatical visit to Princeton University. The first and second authors contributed equally.

## Supplementary material

Supplementary material is available at https://doi.org/10.1017/jfm.2019.503.

## REFERENCES


AZIZ, S. D. & CHANDRA, S. 2000 Impact, recoil and splashing of molten metal droplets. *Intl J. Heat Mass Transfer* **43** (16), 2841–2857.

BEILHARZ, D., GUYON, A., LI, E. Q., THORAVAL, M.-J. & THORODDSEN, S. T. 2015 Antibubbles and fine cylindrical sheets of air. *J. Fluid Mech.* **779**, 87–115.

BIRD, J. C., DE RUITER, R., COURBIN, L. & STONE, H. A. 2010 Daughter bubble cascades produced by folding of ruptured thin films. *Nature* **465**, 759–762.

VAN DER BOS, A., VAN DER MEULEN, M.-J., DRIESSEN, T., VAN DEN BERG, M., REINTEN, H., WIJSHOFF, H., VERSLUIS, M. & LOHSE, D. 2014 Velocity profile inside piezoacoustic inkjet droplets in flight. *Phys. Rev.* A **1**, 014004.

CASTILLO-OROZCO, E., DAVANLOU, A., CHOUDHURY, P. K. & KUMAR, R. 2015 Droplet impact on deep liquid pools: Rayleigh jet to formation of secondary droplets. *Phys. Rev.* E **92** (5), 053022.

CHAPMAN, D. S. & CRITCHLOW, P. R. 1967 Formation of vortex rings from falling drops. *J. Fluid Mech.* **29** (1), 177–185.

DEEGAN, R. D., BRUNET, P. & EGGERS, J. 2007 Complexities of splashing. *Nonlinearity* **21** (1), C1.

DOOLEY, B. S., WARNCKE, A. E., GHARIB, M. & TRYGGVASON, G. 1997 Vortex ring generation due to the coalescence of a water drop at a free surface. *Exp. Fluids* **22** (5), 369–374.

GART, S., MATES, J. E., MEGARIDIS, C. M. & JUNG, S. 2015 Droplet impacting a cantilever: a leaf-raindrop system. *Phys. Rev.* A **3** (4), 044019.

GILET, T. & BOUROUIBA, L. 2015 Fluid fragmentation shapes rain-induced foliar disease transmission. *J. R. Soc. Interface* **12** (104), 20141092.

HSIAO, M., LICHTER, S. & QUINTERO, L. G. 1988 The critical Weber number for vortex and jet formation for drops impinging on a liquid pool. *Phys. Fluids* **31** (12), 3560–3562.

JOSSERAND, C. & THORODDSEN, S. T. 2016 Drop impact on a solid surface. *Annu. Rev. Fluid Mech.* **48**, 365–391.

KUNDU, P. & COHEN, I. 2008 *Fluid Mechanics*. Academic Press.

LENG, L. J. 2001 Splash formation by spherical drops. *J. Fluid Mech.* **427**, 73–105.

MICHON, G.-J., JOSSERAND, C. & SÉON, T. 2017 Jet dynamics post drop impact on a deep pool. *Phys. Rev. Fluids* **2** (2), 023601.

MOREIRA, A. L. N., MOITA, A. S. & PANAO, M. R. 2010 Advances and challenges in explaining fuel spray impingement: How much of single droplet impact research is useful? *Prog. Energy Combust. Sc.* **36** (5), 554–580.

MURPHY, D. W., LI, C., DALBIGNAC, V., MORRA, D. & KATZ, J. 2015 Splash behaviour and oily marine aerosol production by raindrops impacting oil slicks. *J. Fluid Mech.* **780**, 536–577.

NASA, GLENN RESEARCH CENTER 1999 Aerodynmics index: drag of a sphere. https://www.grc.nasa.gov/www/k-12/airplane/dragsphere.html.

PAN, K. L. & LAW, C. K. 2007 Dynamics of droplet–film collision. *J. Fluid. Mech.* **587**, 1–22.

PECK, B. & SIGURDSON, L. 1994 The three-dimensional vortex structure of an impacting water drop. *Phys. Fluids* **6** (2), 564–576.

PROSPERETTI, A., CRUM, L. A. & PUMPHREY, H. C. 1989 The underwater noise of rain. *J. Geophys. Res.* **94** (C3), 3255–3259.

PURVIS, R. & SMITH, F. T. 2005 Droplet impact on water layers: post-impact analysis and computations. *Phil. Trans. R. Soc. Lond.* A **363** (1830), 1209–1221.

REIN, M. 1993 Phenomena of liquid drop impact on solid and liquid surfaces. *Fluid Dyn. Res.* **12** (2), 61.

REIN, M. 1996 The transitional regime between coalescing and splashing drops. *J. Fluid Mech.* **306**, 145–165.

RODRIGUEZ, F. & MESLER, R. 1988 The penetration of drop-formed vortex rings into pools of liquid. *J. Colloid Interface Sci.* **121** (1), 121–129.

SHANKAR, P. N. & KUMAR, M. 1995 Vortex rings generated by drops just coalescing with a pool. *Phys. Fluids* **7** (4), 737–746.

TANG, X., SAHA, A., LAW, C. K. & SUN, C. 2016 Nonmonotonic response of drop impacting on liquid film: mechanism and scaling. *Soft Matt.* **12** (20), 4521–4529.

TANG, X., SAHA, A., LAW, C. K. & SUN, C. 2018 Bouncing-to-merging transition in drop impact on liquid film: role of liquid viscosity. *Langmuir* **34** (8), 2654–2662.

TANG, X., SAHA, A., LAW, C. K. & SUN, C. 2019 Bouncing drop on liquid film: dynamics of interfacial gas layer. *Phys. Fluids* **31** (1), 013304.

THORAVAL, M.-J., TAKEHARA, K., ETOH, T. G. & THORODDSEN, S. T. 2013 Drop impact entrapment of bubble rings. *J. Fluid Mech.* **724**, 234–258.

THORODDSEN, S. T. 2002 The ejecta sheet generated by the impact of a drop. *J. Fluid Mech.* **451**, 373–381.

THORODDSEN, S. T., ETOH, T. G. & TAKEHARA, K. 2003 Air entrapment under an impacting drop. *J. Fluid Mech.* **478**, 125–134.

TRAN, T., DE MALEPRADE, H., SUN, C. & LOHSE, D. 2013 Air entrainment during impact of droplets on liquid surfaces. *J. Fluid Mech.* **726**, R3.

WEHELIYE, H., DONG, T. & ANGELI, P. 2017 On the effect of surfactants on drop coalescence at liquid/liquid interfaces. *Chem. Engng Sci.* **161**, 215–227.

WEISS, D. A. & YARIN, A. L. 1999 Single drop impact onto liquid films: neck distortion, jetting, tiny bubble entrainment, and crown formation. *J. Fluid Mech.* **385**, 229–254.

YARIN, A. L. 2006 Drop impact dynamics: splashing, spreading, receding, bouncing. *Annu. Rev. Fluid Mech.* **38**, 159–192.

ZHAO, H., BRUNSVOLD, A. & MUNKEJORD, S. T. 2011 Investigation of droplets impinging on a deep pool: transition from coalescence to jetting. *Exp. Fluids* **50** (3), 621–635.